An Improved One-Dimensional Bending Angle Forward Operator for the Assimilation of Radio Occultation Profiles in the Lower Troposphere

L. CUCURULL[a] AND R. J. PURSER[b]

[a] *NOAA/Atlantic Oceanographic and Meteorological Laboratory, Miami, Florida*
[b] *IMSG and Lynker at NOAA/NCEP Environmental Modeling Center, College Park, Maryland*

(Manuscript received 22 March 2022, in final form 2 December 2022)

ABSTRACT: Under very large vertical gradients of atmospheric refractivity, which are typical at the height of the planetary boundary layer, the assimilation of radio occultation (RO) observations into numerical weather prediction (NWP) models presents several serious challenges. In such conditions, the assimilation of RO bending angle profiles is an ill-posed problem, the uncertainty associated with the RO observations is higher, and the one-dimensional forward operator used to assimilate these observations has several theoretical deficiencies. As a result, a larger percentage of these RO observations are rejected at the NWP centers by existing quality control procedures, potentially limiting the benefits of this data type to improve weather forecasting in the lower troposphere. To address these problems, a new methodology that enables the assimilation of RO data to be extended to the lower moist troposphere has been developed. Challenges associated with larger atmospheric gradients of refractivity are partially overcome by a reformulation that has minimal effect at higher altitudes. As a first step toward this effort, this study presents both the theoretical development of this new methodology and a forecast impact assessment of it using the NCEP NWP system. Though using a conservative approach, benefits in the lower tropical troposphere are already noticeable. The encouraging results of this work open the potential for further exploitation and optimization of RO assimilation.

KEYWORDS: Global positioning systems (GPS); Remote sensing; Satellite observations; Data assimilation

1. Introduction

Over the last few years, radio occultation (RO) remote sensing of the atmosphere has proven to be a significant component of the global observing system in global weather forecasting (Healy and Thépaut 2006; Cucurull and Derber 2008; Aparicio and Deblonde 2008; Rennie 2010; Anlauf et al. 2011; Cucurull et al. 2013; Cucurull and Anthes 2015). The RO technology provides precise and accurate globally distributed thermodynamics profiles with high vertical accuracy and resolution (Kursinski et al. 1997; Rocken et al. 1997; Anthes et al. 2008). RO observations have equal accuracy over land as over ocean, and their assimilation in numerical weather prediction (NWP) models complements and enhances the use of microwave and infrared soundings (Poli et al. 2010; Bauer et al. 2014; Cucurull et al. 2014; Bonavita 2014).

Since the RO technology is minimally affected by clouds, RO profiles penetrate deeper into the lower troposphere, making this technique well suited for probing the marine planetary boundary layer (PBL). A realistic representation of the PBL is necessary to better understand the processes governing the energy exchanges between the free troposphere and Earth's surface (Garratt 1994). Analyses and forecasts of the PBL from weather and climate models are far from optimal (e.g., Duynkerke and Teixeira 2001; Soden and Held 2006).

Even though RO technology is a promising tool in recovering the PBL structure, operational NWP centers are rejecting a large percentage of RO observations at and below[1] the top of the PBL, potentially limiting the benefits of this data type to improve weather forecasting in the lower troposphere (Poli et al. 2009; Anlauf et al. 2011; Cucurull 2015). The reason for rejection in these cases is that, near very large vertical gradients of atmospheric refractivity, the downward bending curvature exceeds the curvature of the local geoid. This condition is known as super-refraction (SR) or ducting. A special case of SR occurs for rays striking SR layers at glancing incidence angles. Observations from these special cases are unusable because either the rays incur too much bending to reach the receiver at all, or else are too scattered and attenuated by their excessively long residence in the horizontally inhomogeneous ducting region to provide a usable signal once they emerge. However, rays penetrating an SR layer at nonglancing incidence angles are affected by the SR layer, but still contain useful information. This condition frequently occurs at the top of a tropical maritime PBL layer (Von Engeln and Teixeira 2004) and over western coasts of major continents (Xie et al. 2010; Feng et al. 2020) owing to the abrupt negative vertical gradients of humidity often found there.

The existence of an SR layer within the sampled vertical profile presents several serious challenges when attempting to assimilate the RO observations into NWP models (Sokolovskiy 2003; Xie et al. 2006). Under atmospheric SR conditions, the assimilation of bending angle soundings in NWP is undetermined or ill-posed, meaning that an infinite number of

Corresponding author: Lidia Cucurull, Lidia.Cucurull@noaa.gov

[1] In this paper, directional qualifiers (e.g., above, below, top, bottom) are in the sense of an altitudes or height coordinate system.

DOI: 10.1175/MWR-D-22-0073.1

atmospheric states are consistent with a given unique vertical RO profile. In addition, the uncertainty associated with the retrievals is higher. Finally, and in addition to errors induced by neglecting the horizontal gradients of refractivity in the atmosphere, the one-dimensional forward operator used to simulate bending angle profiles from model variables has several deficiencies. Hereafter we will refer to the challenges of current NWP practices to assimilate or reject RO observations affected by SR as NWP data assimilation (DA) challenges (NWP DA challenges). Existing quality controls identify and discard observations that might be affected by atmospheric SR conditions.

NWP DA creates an optimal analysis of the state of the atmosphere by combining prior information with the difference between observations and the forward model estimate of the observable (i.e., the innovations). The prior information is the short-term forecast or background atmospheric state. During DA, the RO forward operator calculates an estimate of the observation by transforming the prior atmospheric state to the atmospheric state along the RO ray to the refractivity to the bending angle to the time delay, stopping at whichever of atmospheric state, refractivity, bending angle, or time delay is taken to be the observable. NWP DA systems prefer to use bending angle as the observable due to issues that arise when processing the raw RO observations to time delay, refractivity, and atmospheric state. First, the retrieval of atmospheric state profiles from refractivity or bending angles is ill-posed under all conditions and auxiliary atmospheric state information must be used to define a well-posed problem. The use of this auxiliary atmosphere state information would adversely affect the DA. Second, although the retrieval of refractivity profiles from bending angles is well-posed (Hajj et al. 1994) with the use of an Abel transform (Fjeldbo et al. 1971), this method results in refractivity values negatively biased at and below the PBL height because the Abel transform does not recover the refractivity structure within the SR region (Feng et al. 2020). Third, the use of time delays is an unnecessary complication when the atmospheric state is assumed to be horizontally homogeneous, which is a sufficient approximation at the scales of global NWP.

A Constellation Observing System for Meteorology, Ionosphere, and Climate (COSMIC) follow-on mission, COSMIC-2, was successfully launched into equatorial orbit on 24 June 2019 (Schreiner et al. 2020; Ho et al. 2020). With an increased signal-to-noise ratio due to improved receivers and digital beam steering antennas, COSMIC-2 is producing about 5000 high-quality RO profiles daily over the tropics and subtropics. Furthermore, it has been demonstrated that COSMIC-2 is able to detect atmospheric SR conditions (Schreiner et al. 2020). Operational weather centers have shown positive benefits from the assimilation of COSMIC-2 soundings, with larger impacts found in the tropical latitudes (Ruston and Healy 2021; Lien et al. 2021).

Profiles from the COSMIC-2 mission began to be operationally assimilated at NOAA in May 2020, a bit later than at the U.S. Naval Research Laboratory (NRL; December 2019) and the European Centre for Medium-Range Weather Forecasts (ECMWF; March 2020). However, benefits from COSMIC-2 at NOAA were lower than those found at other centers and lower than what would be expected from recent observing system simulation experiments (Cucurull and Mueller 2020; Cucurull and Casey 2021). Therefore, optimization of COSMIC-2 assimilation at NOAA was warranted, and ongoing work has been done since the operational implementation, and progress has been made to mitigate existing NWP DA challenges. Overall, optimizing the assimilation algorithms for RO soundings in the lower tropical troposphere is critical to fully exploit the benefits that COSMIC-2 and future RO missions will bring to the NWP community.

NOAA National Centers for Environmental Prediction (NCEP) are currently assimilating RO-derived bending angle observations in their operational global NWP data assimilation system (Cucurull 2010; Cucurull et al. 2013). Updated algorithms to better quality control RO profiles under SR atmospheric conditions were implemented operationally at NCEP in 2015 (Cucurull 2015). It is important to emphasize that the rejection of lower-altitude observations due to SR conditions is not based on the value of the differences between the observations and their simulated values, which is already addressed by standard quality controls, but on whether model conditions are SR or close to SR, regardless of the magnitude of the differences between observed and simulated values. There is currently no information on whether an observation has been affected by actual atmospheric SR conditions, so existing quality controls make use of model vertical refractivity gradient information.

We have developed, implemented, and tested an improved one-dimensional bending angle forward operator to investigate the usefulness of RO profile information for NWP applications below layers of larger vertical gradient of refractivity, including below SR layers. This new formulation should result in a better characterization of the PBL and potentially improve forecast skill in the lower troposphere, especially for the tropical maritime boundary layer. Corresponding tangent linear and adjoint codes associated with the new formulation were also developed. A theoretical description of this advanced forward operator, as well as an example of a practical implementation and forecast skill impact assessment in the NCEP global NWP system, are the focus of this manuscript. An early version of the forward operator component of this new methodology was used to improve the generation of synthetic RO profiles in the most recent observing system simulation experiment with COSMIC-2 at NOAA (Cucurull and Casey 2021).

To the best of our knowledge, we present in this paper the first attempt to implement a methodology to improve the assimilation of low-altitude bending angle observations under large vertical gradients of atmospheric refractivity including, but not limited to, SR conditions. In the closest published precursor study, Xie et al. (2006, hereafter X06) developed a technique to reconstruct RO refractivity profiles from bending angle profiles within the marine boundary layer. When the presence of an SR layer can be identified, the X06 technique results in improved retrievals of refractivity profiles in the lower troposphere. The X06 reconstruction method assumes that the height of the upper limit of the SR layer and the value of the refractivity close to the surface can be

independently obtained. Though the X06 approach could potentially be used to improve the assimilation of refractivities by using more accurate retrievals within the marine boundary layer (Wang et al. 2017), most operational NWP centers now directly assimilate profiles of bending angle rather than soundings of refractivity. Furthermore, it is unclear how the occurrence of model SR conditions would be handled when assimilating X06 reconstructed refractivities.

This paper is organized as follows. Section 2 reviews SR atmospheric conditions and their implications for NWP applications. Section 3 investigates the limitations of NOAA's operational NCEP's bending angle method (NBAM) RO forward operator under large vertical gradients of refractivity. Section 4 introduces the new NCEP's advanced bending angle method (NABAM) RO forward operator, and section 5 analyzes stand-alone cases. Section 6 presents results from a preliminary practical implementation of this enhanced methodology in the NCEP global NWP configuration. Finally, section 7 summarizes the main findings and future work.

2. Atmospheric super-refraction and implications for NWP

In geometric optics, and under the assumption of spherical symmetry of the atmospheric refractivity n, a ray satisfies Bouguer's rule (Born and Wolf 1964):

$$rn(r)\sin\varphi = a, \tag{1}$$

where, for a given ray, the impact parameter a is a constant, r is the radius from the center of Earth to a point on the ray, and φ is the angle between the ray path and the radial direction from the center of symmetry. The bending angle is symmetric with respect to the tangent point r_t (the value of r when $\varphi = 90°$), and the accumulated bending angle can be expressed as follows (Tatarskiy 1968; Fjeldbo et al. 1971):

$$\alpha(r_t) = -2r_t n(r_t)\int_{r_t}^{\infty} \frac{dn/dr}{n(r)\sqrt{r^2n^2(r) - r_t^2n^2(r_t)}}dr. \tag{2}$$

Applying a change of variable $x = rn(r)$ and $r_t n(r_t) = a$, (2) can be rewritten as

$$\alpha(a) = -2a\int_a^{\infty} \frac{d\ln n/dx}{\sqrt{x^2 - a^2}}dx. \tag{3}$$

The change of variable and hence (3) assumes that the refractional radius $x(r)$ is a monotone function and, therefore, there is a unique radius r_t that verifies $r_t n(r_t) = a$. The index of refraction can then be obtained by applying an Abel transform to (3):

$$n(x) = \exp\left[\frac{1}{\pi}\int_x^{\infty} \frac{\alpha(a)da}{\sqrt{a^2 - x^2}}\right]. \tag{4}$$

Typically, in the atmosphere $dn/dr < 0$ and $dx/dr > 0$. However, when $dn/dr < -n/r$ or when the vertical gradient of refractivity N, where $N = (n - 1) \times 10^6$, exceeds the critical value of $dN/dr < -157$ N-unit km^{-1}, then $dx/dr < 0$. This condition is known as atmospheric SR or ducting. Under SR conditions, the radius of curvature of the ray at the tangent point is smaller than the radius of curvature of the geoid at the tangent point (i.e., local geopotential curvature) and, as a result, rays with tangent point inside an SR layer are internal (i.e., they do not start and end outside the atmosphere). Externals rays (i.e., rays that start and end outside the atmosphere) might cross an SR layer, but their tangent point will be outside the layer (Sokolovskiy 2003). Furthermore, when SR occurs, $x(r)$ is no longer a monotone function and the normal condition $a = r_t n(r_t)$ no longer corresponds to the external ray with impact parameter a. That is, there is an infinite number of tangent points r_i for each internal ray that verify $a = r_i n(r_i)$ (Xie et al. 2006), which results in the NWP DA challenges when profiles of bending angle are used below an SR layer.

Since the unique correspondence between r_t and a is not valid under SR conditions, (4) is not applicable and its use results in a negatively biased refractivity value inside and below the SR. This negative bias is due to the lack of external rays within the SR layer—so the contribution of this layer is not accounted for when reconstructing the refractivity structure. The bias is not due to the numerical singularity in a, which can be computed as accurately as needed. Equation (4) is only applicable for external rays.

As the tangent point of a ray approaches an SR layer during an occultation event, the bending angle cumulatively increases to extremely large numbers. The bending angle becomes well defined again below the *shadow* layer, which is the layer below the SR layer where $x(r)$ becomes monotone again. Also, note that since (3) peaks at the tangent point height, the contribution of an SR layer to the bending angle value for an external ray that crosses an SR layer will decrease as the tangent point within a RO profile descends away from the SR layer.

Figure 1a shows, schematically, the effect of an SR layer on a bundle of rays in a vertical plane artificially (and impossibly) arranged to all have horizontal tangents as they pass the same central location of the diagram, where there is assumed to be a horizontally uniform refractivity distribution with a simulated layer of super-refractivity just above 1 km above ground. The altitude of each simulated ray is shown relative to the horizontal, which is plotted here with its own constant curvature removed so that the integrated ray paths exhibit a parabolic form in the absence of the additional refractive bending. The additional bending forced by the vertical gradient of the refractive index at each point along the ray allows its path to be traced numerically by a double integration of this bending added to the aforementioned constant parabolic curvature. Rays above and below the SR layer escape to space in both right and left directions (external rays), while those starting in the SR layer remain trapped within it. A more realistic cartoon for RO is shown in Fig. 1b for the same idealized refractivity profile used in Fig. 1a. Rays enter from space at the left, starting nearly parallel, and almost all return to space, but some spend a very long time in the SR layer before eventually escaping. These rays will accumulate extremely large bending angles and would not provide any useful information. Therefore,

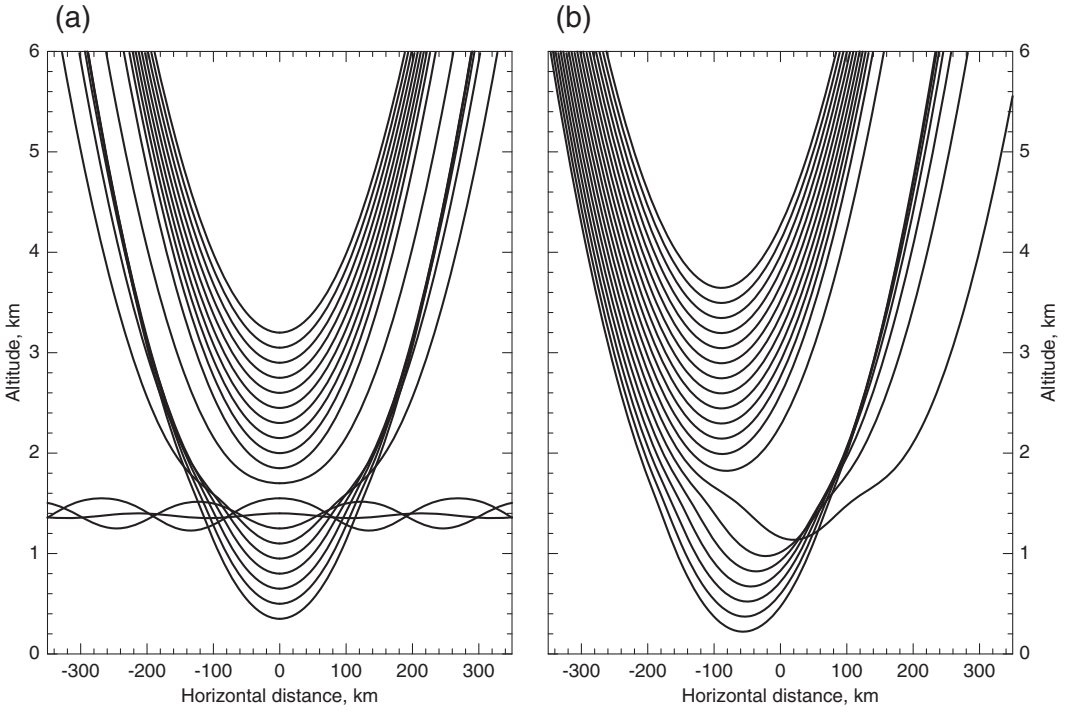

FIG. 1. (a) Cartoon representing the effect of a super-refraction layer on a bundle of rays artificially arranged in a vertical plane to be instantaneously horizontal as they pass through the vertical midline. (b) A more pertinent cartoon for radio occultation observations and for the same idealized refractivity profile. Rays enter from space at the left, starting nearly parallel, and almost all return to space, but some spend a very long time in the SR layer before eventually escaping.

they must be excluded from data assimilation if they are observed at all. However, rays penetrating the SR layer more steeply, with tangent points far enough below the SR layer, might be usable in NWP as they offer valid opportunities for assimilating thermodynamic quantities at these meteorologically important altitudes.

NCEP uses a forward operator based on (3) to assimilate RO data (NBAM; Cucurull et al. 2013), and this function has a singularity in a within the SR layer. In geometric optics, the singularity in $\alpha(a)$ is because the gradient of refractivity exceeds the critical gradient value and not due to the lack of external rays within the SR layer. In fact, if SR would occur at a single point rather than in a layer (i.e., no presence of internal rays), the singularity in $\alpha(a)$ would still exist at that point.

When SR occurs, there is an infinite number of retrieved atmospheric (refractivity) structures within the SR layer that correspond to the same bending angle profile (Xie et al. 2006). The real structure within this layer is unknown, causing NWP DA challenges when bending angle observations are used below the SR layer. The assimilation of bending angles using NBAM, or any other forward operator based on (3), in NWP affected by SR results in multiple local minima in the observation cost function, each solution corresponding to one of the compatible atmospheric state solutions. Even worse, these minima are not well separated.

Current NCEP quality controls techniques address both the situation where atmospheric SR might have contaminated the observations, as well as the situation when there is SR in the background field evaluated at the location of the observation. When this occurs, the one-dimensional forward operators based on (3), such as NBAM, have a singularity in the SR layer and, as with the assimilation of observations affected by atmospheric SR, their use in data assimilation is ill-posed below the model SR layer.

At NCEP, SR quality control procedures were implemented to detect and reject observations under the presence of larger atmospheric refractivity vertical gradients, including, but not limited to, SR conditions (Cucurull 2015). Briefly, a model SR flag checks for large values of the model vertical gradient of refractivity (75% of the critical value) in the vicinity of an RO observation to identify issues in the simulation of an RO observation. A second observation SR flag checks for larger values of observed bending angles ($\geq$0.03 rad) in combination with larger model vertical gradients of refractivity (50% of the critical value). An observation is rejected when either of these two situations occurs. Note that these checks detect and reject observations under the presence of larger atmospheric refractivity vertical gradients, including, but not limited to, SR conditions.

Despite the uncertainty associated with bending angles below an atmospheric SR layer, these observations contain information on the thermodynamic state of the atmosphere. By appropriately weighting the NWP background field in data assimilation, it might be possible to constrain the analysis

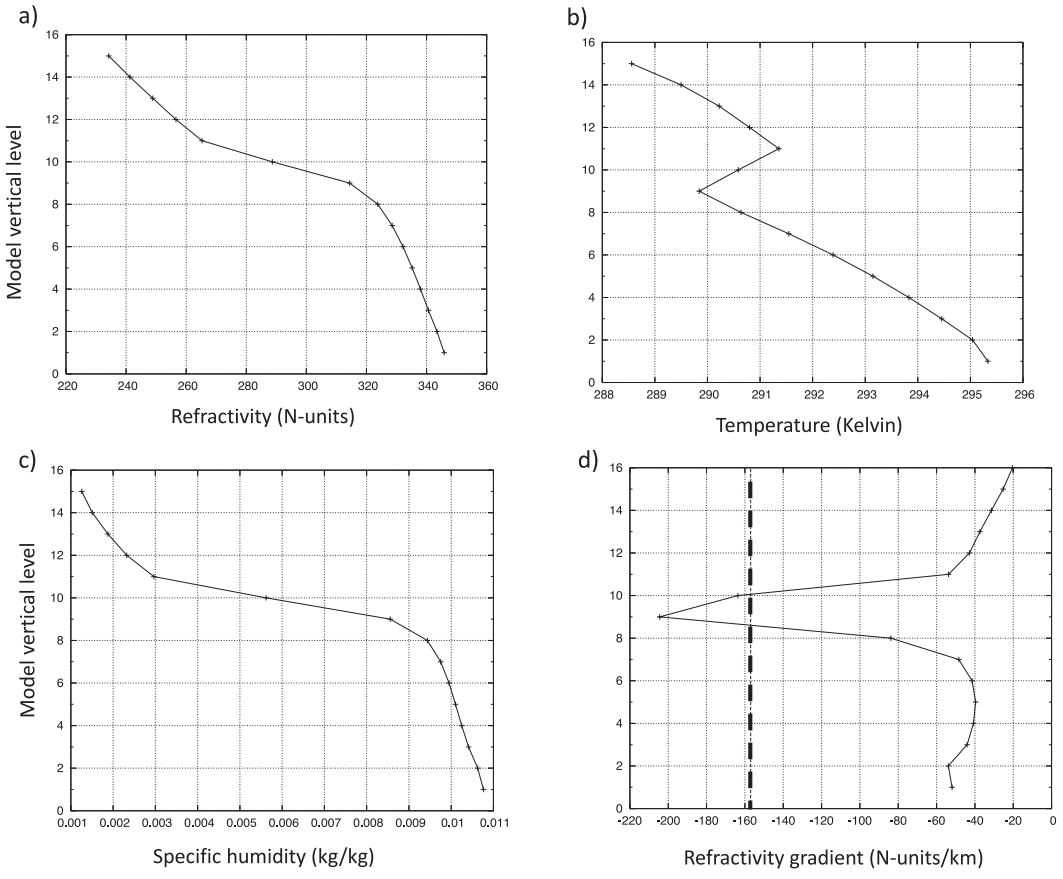

FIG. 2. (a)–(d) Model vertical structure for a two-layer super-refraction case. The dashed vertical line in (d) indicates critical refraction.

toward the true atmospheric state—thus choosing the optimal solution among the infinite number of potential solutions. The same approach can be adopted when applying (3) under model SR conditions. Investigating the value, if any, gained from assimilating bending angle observations below an atmospheric or model SR using the background field as an external constraint is investigated in this study.

Figures 2a–d provide an example of SR conditions detected in NCEP's model. Here, the vertical gradient of refractivity exceeding the critical gradient extends to two model layers. A sharp temperature inversion (Fig. 2b) and a strong negative moisture gradient (Fig. 2c) result in a very large refractivity gradient, as depicted in Fig. 2d. The RO technology is sensitive to the vertical structure of the gradient of refractivity caused by strong inversion layers.

3. NBAM limitations under large vertical gradients of refractivity

Typically, operational NWP centers use a practical implementation of (3) to assimilate RO bending angle observations. For example, NRL uses the one-dimensional operator from the Radio Occultation Processing Package (ROPP), developed under the EUMETSAT ROM-SAF (Burrows et al. 2014; Culverwell et al. 2015) and ECMWF uses a two-dimensional operator (Healy et al. 2007). Neither operator uses bending angle observations below an SR layer due to the NWP DA challenges.

A detailed description of NOAA's operational NBAM forward operator to assimilate bending angle profiles can be found in Cucurull and Derber (2008) and Cucurull et al. (2013). Briefly, this forward operator accounts for the numerical singularity that exists in the denominator of the integrand in (3) by computing the bending angle in a new integration grid parameter s, where

$$x = \sqrt{a^2 + s^2}. \tag{5}$$

This allows the numerical evaluation of the integral in (3) to be executed on an equally spaced grid in s with the integrand no longer possessing a reciprocal-square root singular form at the tangent point, so that the trapezoidal rule can be used without incurring enough of a truncation error to be of any concern. Many other transformations different from the hyperbola implied by (5) that overcome the integrand's singularity at $x = a$ are also possible (only requiring that x–a be locally quadratic in s). These s-indexed values of refractivity must be obtained by suitable vertical interpolations at the target locations implied by each refractional radius x. For a

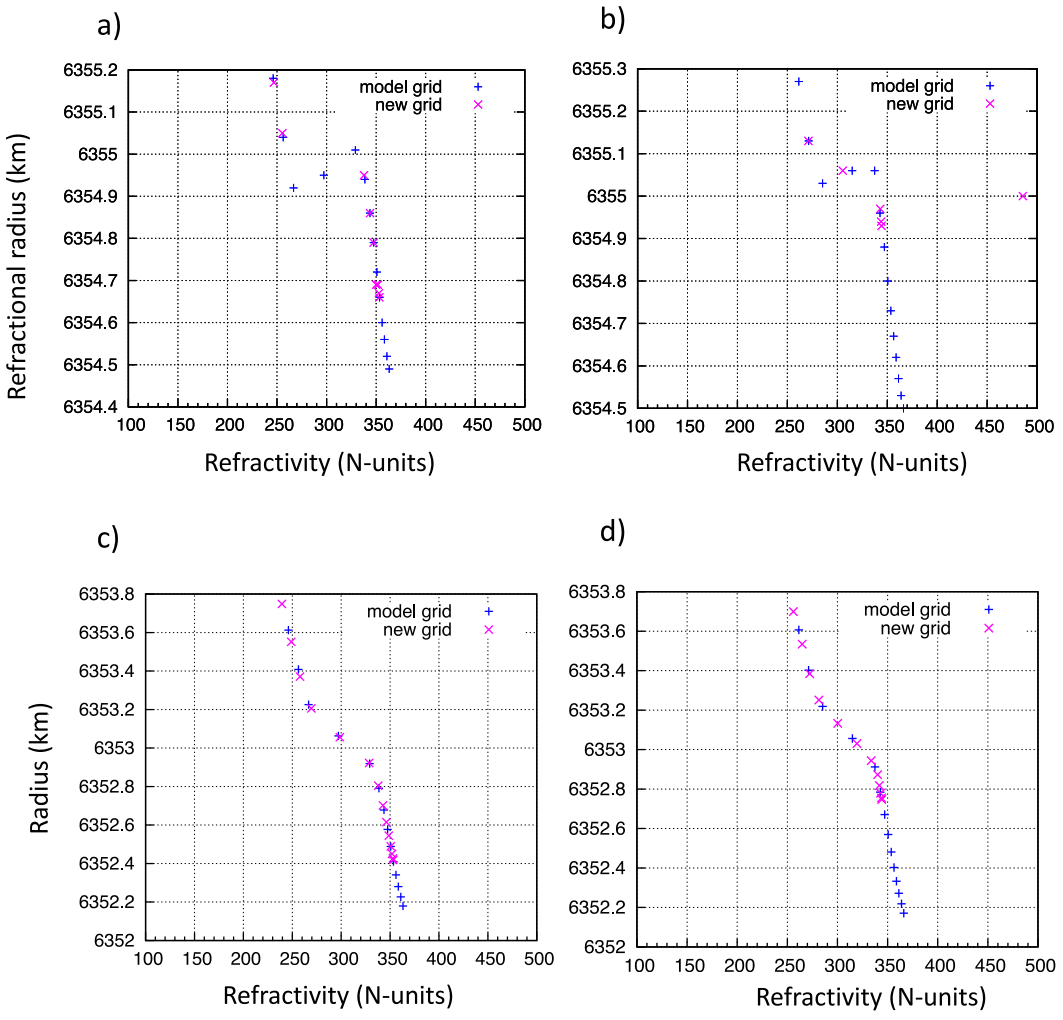

FIG. 3. Examples of discontinuities of NBAM under super-refraction conditions: (a) the ducting layer is not sampled with the new integration grid and (b) a polynomial interpolator is not applicable. Both types of limitations are overcome with the use of NABAM: (c) ducting layer is well sampled and (d) Lagrange interpolators are applicable. Note that NBAM and NABAM use a different height coordinate system (y axis).

target location within a given vertical analysis grid interval, the NBAM uses a linear weighting, over that interval, of the pair quadratic Lagrange polynomials (Abramowitz and Stegun 1970), effecting a cubic interpolation of Hermite type (Johnson and Riess 1982). Each quadratic is fitted to the three grid values centered at each end of the target interval, which ensures continuity of the interpolated refractivity values and their derivatives in both the analysis vertical grid and in the new integration grid s. Note that this methodology requires only the existence of a smooth distribution of the values of the model refractivity on the analysis vertical grid to ensure that the interpolator can be accurately applied.

The forward problem transforms atmospheric humidity and temperature profiles from a short term forecast to corresponding refractivity and then bending angle profiles. When SR conditions do not exist, this calculation is well posed and has a unique solution. However, it has some limitations under SR atmospheric conditions that might result in a misrepresentation of the simulated bending angle. As with any forward operator based on (3), NBAM assumes that the refractional radius $x(r)$ is a monotonic function. Since under SR conditions this statement is no longer valid, its assumption causes a series of problems in our current approach simulating bending angles associated with the NWP DA challenges. First, the location of an observation within the model refractional radius vertical grid, and the location of the new grid with respect to the source (model) grid, are not well defined near the SR layer. This results in discontinuities in the refractivity profile, as the SR region is not appropriately sampled (Fig. 3a). Furthermore, when atmospheric conditions are close to the critical gradient value, even when the extreme limit of SR conditions has not yet been reached, the integration grid in NBAM might not be sufficiently spaced, which limits the applicability of the Hermite interpolator (Fig. 3b). For example, note the unrealistic

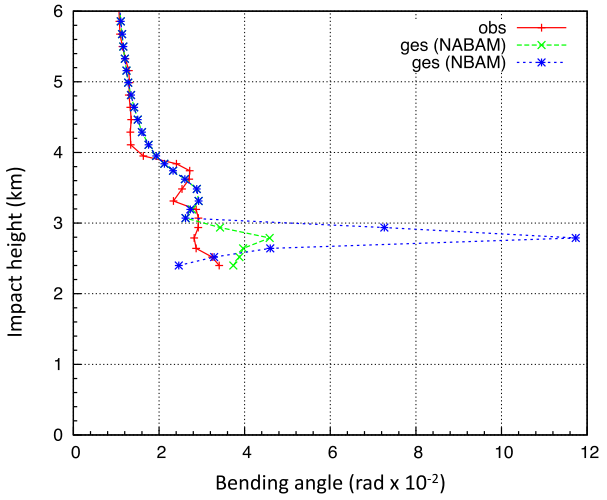

FIG. 4. Bending angle profile and its modeled simulation counterpart with NBAM and NABAM forward operators.

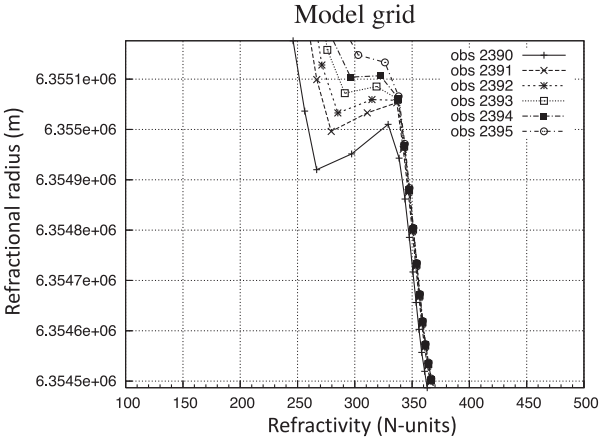

FIG. 5. Modeled refractivity profiles as a function of the refractional radius at the geographical coordinates of six observations belonging to the same radio occultation profile.

value ~480 N-units for one of the points in the new integration plot in Fig. 3b. Rather than rejecting these observations outright, the proposed new NABAM methodology (described and discussed in the next section) solves the challenges associated with the use of the current operator under large vertical gradients of refractivity, including ducting. Limitations of NBAM shown in Figs. 3a and 3b correspond to two observations of the same bending angle profile.

The corresponding bending angle profile is plotted in Fig. 4, where the observed and modeled bending angle profiles for the lowest 6 km of the atmosphere are depicted. The large value in the NBAM modeled profile just below 3 km is unphysical, and it is the result of discontinuities that arise with the implementation of our forward operator when a ray crosses a model SR layer, as shown in Figs. 3a and 3b. It is important to note that Figs. 3 and 4 are just illustrations—when atmospheric SR conditions might exist and unrealistic simulations might occur with NBAM, observations are rejected with the current operational quality control procedures as they typically show larger background innovations.

Since NBAM considers the drift of the tangent point within a profile (Cucurull 2011) not all the observations within a profile might experience SR in their modeling counterpart. As an example, Fig. 5 shows the modeled refractivity as a function of the refractional radius at the location of the lowest six observations of the profile from Fig. 4. Note that the simulated refractivity values for the lowest two observations (2390 and 2391) experience SR in two model layers (10 and 11), as depicted in the figure by the negative vertical gradient of refractivity. On the other hand, observations 2392, 2393, and 2394 only experience one SR layer at model layer 11. Finally, observation 2395 is not affected by model SR.

4. NCEP's advanced bending angle method (NABAM)

Assuming that the refractional radius x is a smooth function of the radius r, we can re-express (3) as

$$\alpha(a) = -2a\int_{r_t}^{\infty} \frac{d\ln n/dr}{\sqrt{x^2(r) - a^2}}\,dr, \tag{6}$$

where r_t is the value that verifies $x(r_t) = a$. The integration grid in (6) is now monotone. Also, since observations within a model SR layer are rejected by the existing quality controls, there is a unique r_t for each impact parameter a. An iterative Newton–Raphson method can be used to estimate r_t from a. A forward operator based on (6) can be used to assimilate observations that are above and below an SR layer, while NBAM can only be used to assimilate observations above a model SR layer.

As in the NBAM approach, we apply a hyperbola-type transformation to remove the singularity at the lower limit of the integral ($r = r_t$):

$$r = \sqrt{r_t^2 + s^2}. \tag{7}$$

Under this transformation, (6) becomes

$$\alpha(a) = -2a\int_0^{\infty} \frac{d\ln n/dr}{\sqrt{r^2[x^2(r) - a^2]/s^2}}\,ds, \tag{8}$$

$$= -2a\int_0^{\infty} \frac{d\ln n/dr}{\sqrt{r^2[x^2(r) - a^2]/(r^2 - r_t^2)}}\,ds. \tag{9}$$

The numerical integration of what is now a smooth integrand, symmetrical about the origin of the new coordinate grid s, fading exponentially fast toward large values of s, can be carried out as it is in the existing NBAM scheme by application of the simple and computationally cheap trapezoidal rule:

$$\alpha(a) = -a\left[\beta_0\Delta s + 2\sum_1^{\infty}\beta_j\,\Delta s\right], \tag{10}$$

with

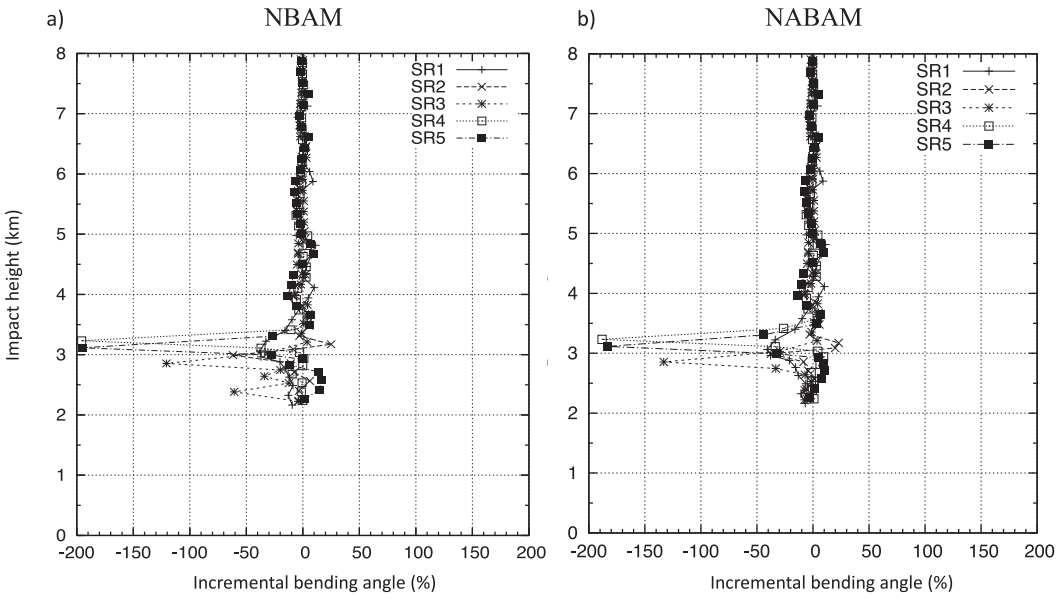

FIG. 6. Differences between the observed and simulated incremental bending angle profiles (in %) for five profiles likely affected by atmospheric super-refraction conditions with the use of (a) NBAM and (b) NABAM forward operators.

$$\beta_j = \left\{\frac{d\ln n/dr}{\sqrt{r^2[x^2(r) - a^2]/(r^2 - r_t^2)}}\right\}_j = \left\{\frac{1}{r}\frac{d\ln n/dr}{\sqrt{[x^2(r) - a^2]/(r^2 - r_t^2)}}\right\}_j. \tag{11}$$

In principle, the linear operations of vertical interpolation of beta from model levels, and the integration with respect to s (which do not change from one iteration of the solver to the next), can be combined and expressed as a simpler and computationally more efficient inner-product of the model level values of beta with a "vector" formed by applying to the s-space "vector" of the quadrature weights implied by (10), the adjoint of the operator vertically interpolating from model levels to s-points.

We then use the approximation:

$$d\ln n/dr \sim 10^{-6} dN/dr, \tag{12}$$

and the Lagrange interpolators in (11) to estimate the refractivity gradient in the new target grid s. The refractional radius x in the new integration grid is computed by applying $x = n(r)r$. The singularity at the tangent point radius in the denominator of (11) is overcome with the use of L'Hôpital's rule, which results in the following expression for β_0:

$$\beta_o = \left[\frac{10^{-6}\left(\frac{dN}{dr}\right)_{r=r_t}}{r_t n(r_t)\sqrt{1 + r_t 10^{-6}\left(\frac{dN}{dr}\right)_{r=r_t}}}\right]. \tag{13}$$

The use of the NABAM scheme based on the formulation in Eq. (6) fixes the discontinuities in the refractivity profile seen in Figs. 3a and 3b. The SR region is now well sampled (Fig. 3c), and the Lagrange interpolators can be correctly applied (Fig. 3d). Previous unphysical bending angles below 3 km obtained with the use of NBAM now show realistic values, while simulated values above this height remain almost the same, regardless of the forward operator used (Fig. 4).

Large differences between observed and simulated bending angles might still exist with the NABAM methodology when a mismatch in PBL height exists between the modeled and observed RO profiles, and these observations will still be rejected with the new methodology. In a bending angle profile, when the radio occultation signal is sensitive to stronger inversion layers observed on top of the convective PBL, the height of the PBL corresponds to a large spike in bending angle caused by larger vertical gradients of refractivity (see, e.g., Ao et al. 2012). However, by improving the simulation of the PBL height (i.e., a better representation of the height of the spike in the bending angle profile), fewer observations would be rejected by existing quality controls that are based on the difference between observations and model simulations. To better illustrate this, it is helpful to make comparisons with the same profiles used in by Cucurull (2015), where Fig. 7a of that study, showing the differences in percentage between modeled and observed values of bending angle for five profiles likely affected by atmospheric SR conditions, is reproduced here as Fig. 6a, while the corresponding results we obtain from the new NABAM method of computing the forward operators are shown in Fig. 6b. Although larger differences still exist in NABAM, the smaller zigzag structures as compared to the use of NBAM (see e.g., profile SR3) indicate that NABAM does a better job at representing the effect of the model PBL on the bending angle which leads to lower bending angle differences below the PBL height.

5. Stand-alone analysis case study

This section investigates the potential impact on the newly developed NABAM methodology for a couple of profiles and compares results with those obtained with current NBAM assimilation algorithms. The corresponding tangent linear and adjoint codes for NABAM were developed and implemented according to the updated forward operator. For this stand-alone testing, a very conservative approach was used in NABAM, and standard quality control assignments were not modified from their default values in NBAM. (Standard quality control values were updated for the forecast skill impact assessment described in section 6.) To address the two SR atmospheric scenarios where larger vertical gradient conditions might either be detected by the model, or potentially be affecting the retrieval of bending angles, an example for each case is presented. Specific technical details for a potential implementation in an operational setting are provided in section 6.

a. *Super-refraction conditions in the model background field*

As an example of how NABAM might enable the potential assimilation of additional observations in the lower troposphere when the model detects larger vertical gradients of atmospheric refractivity, Fig. 7 shows a COSMIC bending angle profile, along with its modeled counterparts with NBAM and NABAM forward operators. For each methodology, model simulations are computed for both the background (or model first guess) and analysis fields. The COSMIC profile under analysis is geographically located in the subtropics (latitude 23°S).

For this profile, the lowest-altitude observation was rejected in both NBAM and NABAM for being located below the lowest model vertical grid. The next six observations below the lowest 3 km flagged the model SR quality control in NBAM and NABAM, indicating that 75% of the critical value was detected within the lowest 6 km of the atmosphere at the geographical latitude and longitude of the observations. The use of the NBAM configuration resulted in a direct rejection of all six observations and the model simulation of the profile stopped at an impact height of 3 km (green curve in Fig. 7). However, five of these observations were located several model layers below their corresponding model SR layer and passed the SR quality control in NABAM for their potential assimilation and contribution to the analysis. The remaining observation was too close to a layer of close-to-SR conditions and was therefore discarded. The simulation of the bending angle profile in NABAM includes these five additional observations (pink curve in Fig. 7). As expected, the corresponding simulated profile from the analysis field also extends lower into the troposphere with the use of the NABAM methodology. Since default quality control procedures were not modified in NABAM, only one (the second lowest) of the five extra observations ended up being actively assimilated–other nonmodel SR quality controls caused the rejection of the rest of the observations. This would explain why the analysis is not closer to the observations ~2.5 km. Small differences between the simulation of the lower-altitude observations as well as in the analysis

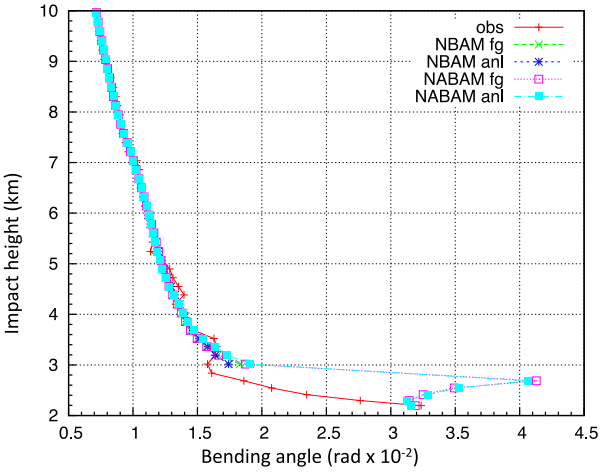

FIG. 7. Bending angle sounding and its modeled simulation counterpart with NBAM and NABAM methodologies for a COSMIC profile that flagged model super-refraction quality controls.

field exist between both approaches above ~3 km. The minimization algorithms behaved well with either methodology.

As expected, the use of the NABAM configuration, along with some additional RO observations enabled in the assimilation algorithms, resulted in changes in the moisture and temperature analyses. The model background, NBAM and NABAM analyses moisture fields interpolated at the location of the radio occultation profile represented in Fig. 7 are shown in Fig. 8a. The model moisture analysis is sensitive to the new assimilation configuration, and small differences are seen between NBAM and NABAM for the lowest few kilometers of the atmosphere. This is also the case for the temperature analysis field in Fig. 8b. Differences between NBAM and NABAM methodologies are evident from the figure, for the lowest 4 km. It is noticeable in the figure that there is a change in the sign with respect to the model background field around 2.8 km. While NBAM results in a warmer analysis, NABAM provides a colder temperature value.

b. *Super-refraction conditions in the soundings of bending angle*

Larger differences between observed and simulated bending angle values might exist with NBAM when observations are flagged as potentially being contaminated by large atmospheric vertical gradients of refractivity in the retrieval process. We analyze here the differences between NBAM and NABAM in handling this situation, and the potential impact of carefully assimilating some of these observations with the NABAM approach. When observations under these conditions are allowed to move forward throughout the assimilation algorithms for their potential contribution to the analysis, their corresponding observation errors are increased due to their larger uncertainty.

As an example, Fig. 9 shows another COSMIC profile (latitude 16°S) where some of the lower-altitude observations flagged the observation SR quality control. This check identifies

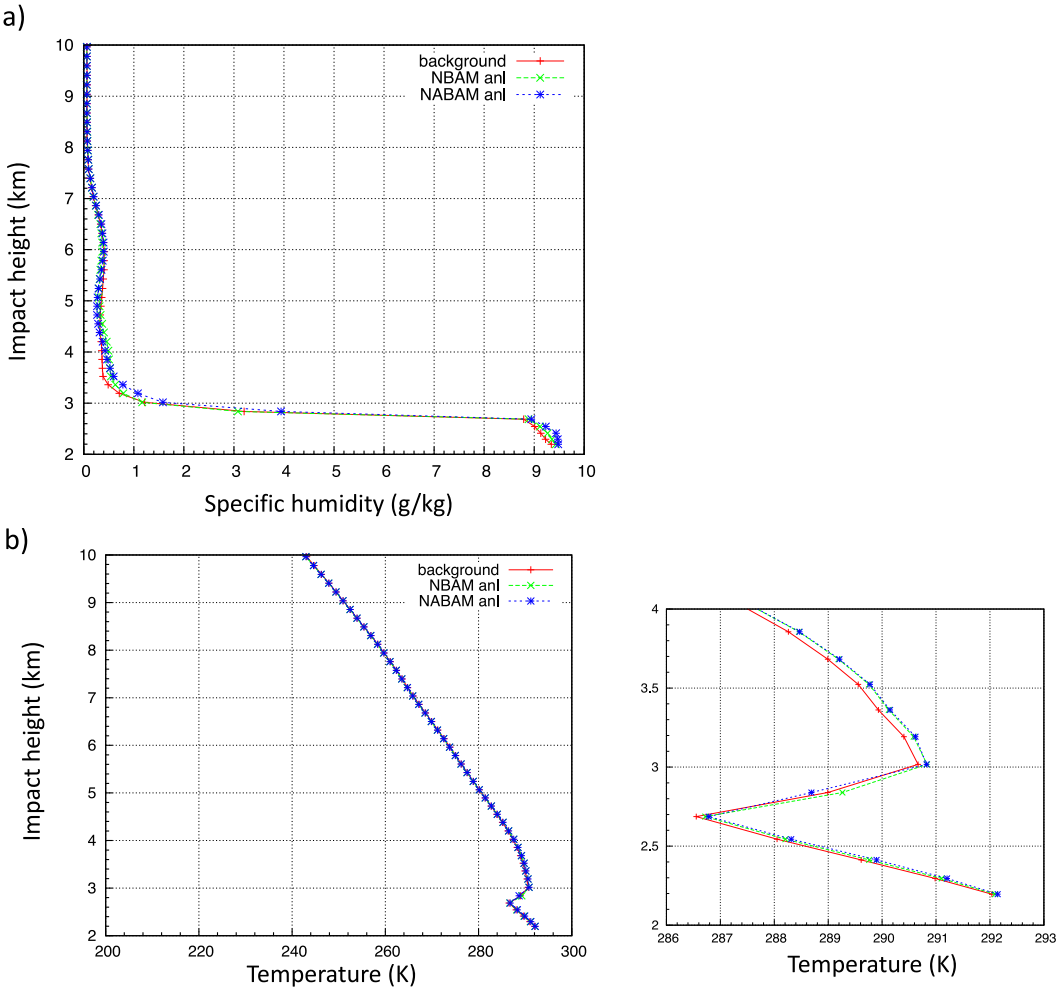

FIG. 8. First guess (background) and NBAM and NABAM (a) moisture and (b) temperature analysis fields interpolated at the location of the bending angle profile from Fig. 7. The smaller box in (b) zooms into the lowest 4 km to detail differences between the three curves.

observations for which the model reaches 50% of the critical gradient value surrounding the location of the observation and the retrieved bending angle value is ≥0.03 rad. For this profile, the model did not detect SR conditions at the location of any of these observations (i.e., only one of the two SR quality controls was flagged), which allows us to isolate the effects of potential SR conditions in the observations. Modeled values with the use of NBAM (green curve) and NABAM (pink curve) for the entire vertical profile below 10 km are shown in Fig. 9. This COSMIC profile (red curve) shows spikes in bending angle at several vertical heights that are not well captured by the modeled simulation counterpart, showing overall smoother vertical structures. Although differences exist between the NBAM and NABAM simulations, neither seem to accurately represent the larger spikes observed at 4 and 5 km. Both approaches appear to show a higher PBL height as compared to the observations, as indicated by the higher height of the larger vertical gradient in bending angle just below 4 km. The NABAM methodology picks up some of the lowest-altitude observations rejected in NBAM. The resulting analysis structures show differences between the NBAM (blue curve) and NABAM (cyan curve) methodologies. NABAM does a better job in capturing the larger magnitude of the bending angle spike observed at around 5.2 km than when NBAM is used. However, NBAM seems to capture the height of this larger spike a bit better (shown at 4.5 km in NABAM versus 5 km in NBAM). The use of the lower-altitude observations in NABAM results in an overall shape of the bending angle profile closer to the observed profile.

As expected, differences in moisture and temperature analysis fields exist between both methodologies as well. When compared to the background field interpolated at the observation's locations (Fig. 10a), NABAM allows for larger moisture increments. Small differences in temperature analyses are shown in Fig. 10b.

6. Example of a practical implementation in NWP

The previous section illustrated some differences in the background and analyses increments as a result of using the

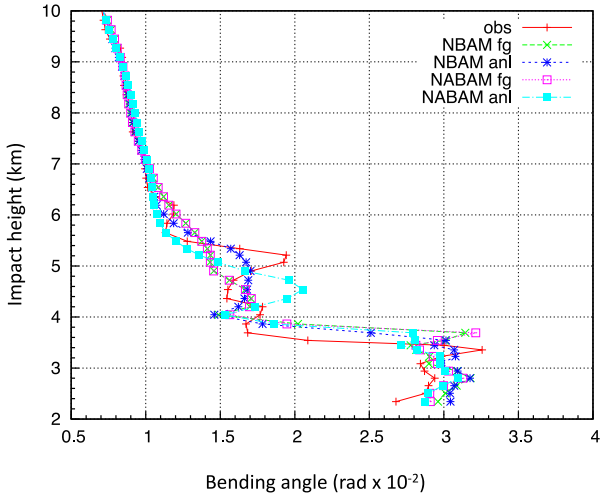

FIG. 9. Bending angle sounding and its modeled simulation counterpart with NBAM and NABAM methodologies for a COSMIC profile that flagged observation super-refraction quality controls.

two assimilation strategies, including the potential use of a few additional observations in the lower troposphere in the NABAM configuration. In this section, we propose a preliminary practical implementation of the NABAM configuration for potential NWP applications. For this purpose, a conservative approach is adopted. While some modifications of current observation error and quality control assignments, including those based on background innovation values, have been implemented for these experimental tests, full optimization of the new methodology with updated observation error and quality control procedures will be developed in future investigations.

For these tests, a hybrid NBAM-NABAM approach was implemented and evaluated. This hybrid approach applies the NBAM forward operator for the first outer loop of the minimization. Low-altitude (≤3 km) observations that flag model and/or observation SR quality controls make use of the NABAM forward operator in the second outer and corresponding inner loops—all other observations are processed with NBAM. In this case, observations that are far below a model layer with a large gradient of vertical refractivity are allowed to proceed further into the assimilation algorithms—this is not the case with the use of NBAM or any other existing bending angle forward operator, where observations below such a layer are directly discarded and prevented from being assimilated. When an observation flags the SR quality control with the use of NABAM in the second outer loop, its corresponding error is inflated according to the expected larger observation error under atmospheric ducting conditions. For this first set of trials, errors were doubled, but optimal values will be tuned in future work. The motivation for this hybrid approach is that by enabling the assimilation of a few additional observations in the second outer loop, they might contribute to the analysis by producing a small correction to the analysis obtained at the end of the first outer iteration, minimizing potential ill-conditioning issues. This hybrid approach also allows the use of approximated algorithms for the NABAM tangent linear code, where the estimated value of the radius at the ray tangent point (height coordinate in the NABAM methodology) within the model vertical grid is fixed in the inner loop. This is consistent with the approach currently adopted for the assimilation of other observations.

In addition to enabling the potential use of observations below a layer of large vertical gradient of refractivity, the new methodology does a better job in representing bending angle profiles in the lower moist troposphere, where larger vertical gradients of refractivity are typically commonly observed in the atmosphere. In these cases, NABAM has the potential of assimilating additional observations that would otherwise be immediately rejected with current quality controls based on background innovation values. Therefore, we were also able to slightly relax the standard quality controls in NABAM for COSMIC-2 since this mission is only sampling the tropical and subtropical latitudes. (Earlier assessment of COSMIC-2 at NCEP had showed some negative impact that was overcome by tightening the quality control procedures for this mission. With the use of the hybrid configuration, we were able to revert to the default quality controls for COSMIC-2 without causing any harm to the system.) Finally, and since the current RO technology is not capable of measuring very large bending angles because of how low (in line-of-sight altitude) we are tracking the transmitter satellites (C. Ao 2022, personal communication), a quality control is implemented in NABAM to reject observations with corresponding forward model estimates larger than 0.05 rad to avoid the assimilation of negatively biased bending angle observations.

For these preliminary tests, we used the 2022 configuration of NCEP's operational data assimilation system (Version 16.1.4), with a finite-volume cubed-sphere dynamical core (FV3GFS; Lin 2004; Lin et al. 2017) and the four-dimensional ensemble variational (4DEnVar) version of the NCEP's Gridpoint Statistical Interpolation (GSI) analysis system. Experiments were run at the lower horizontal research resolution of C384 (~25 km) for the forecast model and C192 (~50 km) for the analysis and ensemble runs. The number of vertical levels was kept the same as in the operational configuration (128). In total, 20 reduced-resolution ensemble members were used to estimate background error covariance via the ensemble Kalman filter. A CONTROL experiment assimilated all the available conventional and satellite observations with the current NBAM configuration. The hybrid NABAM methodology replaced NBAM in the NABAM_HYB experiment. In both cases, the FV3GFS model produced daily extended 192-h global forecasts initialized at 0000 UTC. Experiments were run from 15 December 2020 to 16 January 2021. Verification was done for 20 December–16 January, while the first 5 days were used as a spinup period. (Note that since the statistical package that NCEP uses for verification ignores serial correlation among the forecasts, actual confidence levels might be slightly lower than the 95% provided in the figures.) The RO missions assimilated include *MetOp-A*/*B*/*C*, *TerraSAR-X*, *Tandem-X*, COSMIC-2, *KOMPSAT-5*, GeoOptics, and Spire.

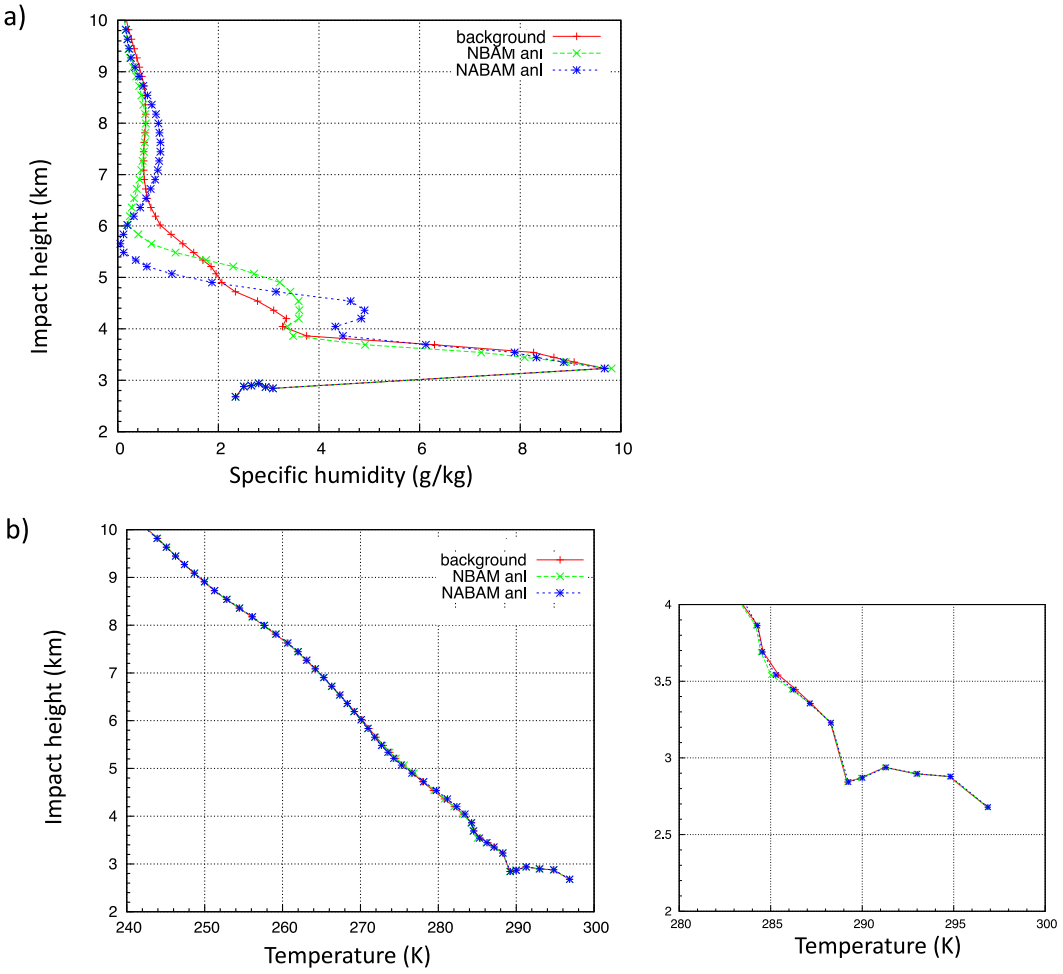

FIG. 10. First guess (background) and NBAM and NABAM (a) moisture and (b) temperature analysis fields interpolated at the location of the bending angle profile from Fig. 9. The smaller box in (b) zooms into the lowest 4 km to detail differences between the three curves.

The overall number of total assimilated RO observations in CONTROL was ~78% and a bit larger (~83%) in NABAM_HYB. This increase was primarily due to the larger number of COSMIC-2 observations assimilated in NABAM_HYB (~89%) versus a value of ~81% in CONTROL. The number was slightly lower for the MetOp satellites in either experiment (~74%) because these profiles are rejected below 8 km due to slightly higher biases. (All the percentages are relative to the number of observations that were already quality-controlled by the processing centers.) The contribution of the assimilation of observations below a layer of large vertical gradient of refractivity in NABAM_HYB only accounted for an increase of ~1% over the counts in CONTROL. As an example, Figs. 11 and 12 show the total number of assimilated observations and the percentage of assimilated observations below 50 hPa, respectively, for 0000 UTC 25 December 2020. As can be seen in the figures, not just the percentage of assimilated observations is higher for COSMIC-2 in NABAM_HYB, but so is the percentage for all the other RO missions below 600 hPa. Since the quality control procedures were only relaxed in NABAM_HYB for COSMIC-2, the new methodology results in more observations contributing to the analysis.

Global ECMWF analyses were used to verify the forecasts from CONTROL and NABAM_HYB analyses. Both experiments showed similar forecast skill in the extratropics and at midupper atmospheric levels. However, some positive effects with the use of the new methodology in NABAM_HYB were noticeable in the lower tropical troposphere. As an example, Figs. 13a and 13b show results for the 850 and 700-hPa root-mean-squared temperature error as a function of the forecast lead time. Impact from the assimilation of the extra few observations in NABAM_HYB results in a reduction of the temperature errors for all forecast lead times, with differences being statistically significant for the first 72 h and at 192 h at the 850-hPa pressure level, and at days 4 and 6 at the 700-hPa pressure level. Though RO only contains direct information on the mass field, indirect impacts on the wind field can be obtained through the model background error covariances. Indirect

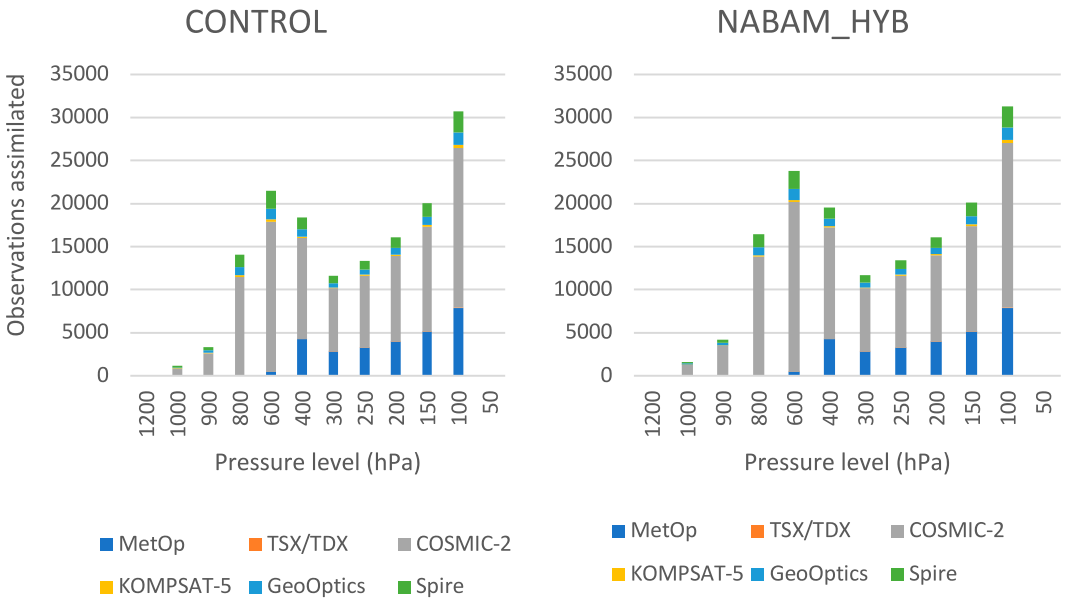

FIG. 11. Total number of observations assimilated on 25 Dec 2020, as a function of the pressure level and radio occultation mission. The pressure level value corresponds to the lower-altitude pressure level of the bin (i.e., values plotted at 600 hPa fall in the 600–400-hPa bin). The highest-altitude pressure value shown in the figure is 50 hPa.

impact from RO also includes improved satellite radiance assimilation through optimized variational bias correction (Poli et al. 2010; Bauer et al. 2014; Cucurull et al. 2014; Bonavita 2014). From our test, a small reduction of the 3-day root-mean-squared wind error in the lower tropical troposphere was also achieved with the use of the new methodology (Figs. 13c,d). Furthermore, the 3-day wind bias at 850 hPa was reduced by ~10% in NABAM_HYB as compared to CONTROL (not shown).

7. Conclusions

While the use of RO data in improving the understanding and predictability of weather and climate grows, there remains

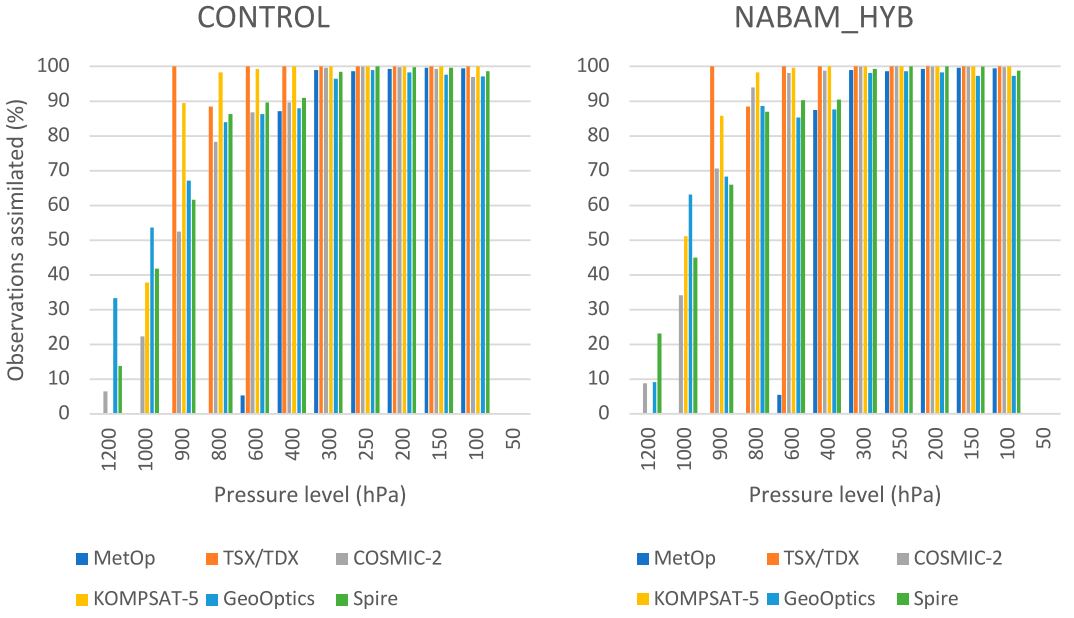

FIG. 12. Total number of observations assimilated (in %) on 25 Dec 2020, as a function of the pressure level and radio occultation mission. The pressure level value corresponds to the lower-altitude pressure level of the bin. The highest-altitude pressure value shown in the figure is 50 hPa.

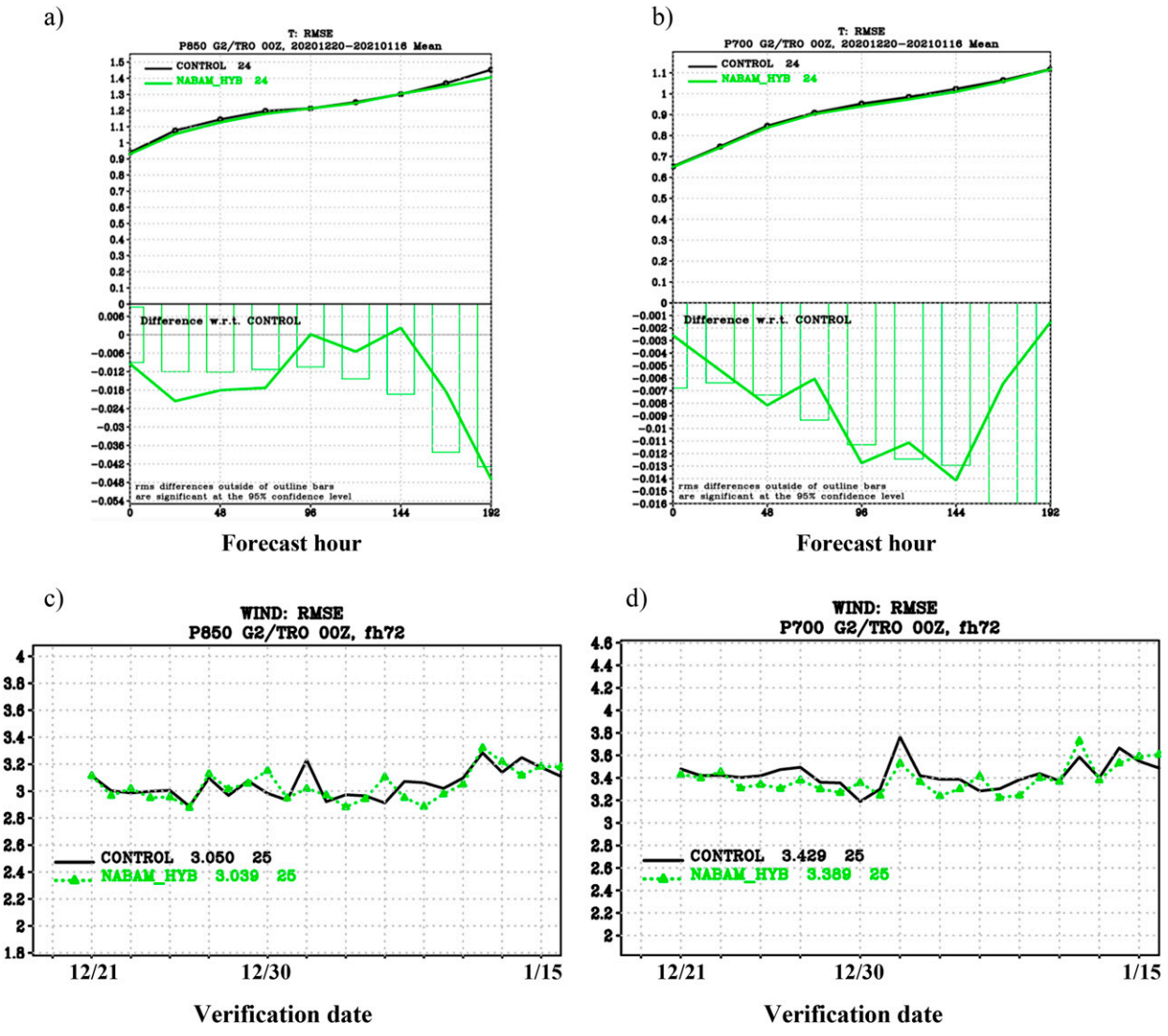

FIG. 13. Root-mean-squared temperature errors in the tropics for the (a) 850- and (b) 700-hPa pressure levels as a function of the forecast lead time. The lower plots in each panel show differences with respect to CONTROL, with negative being an improvement. Bars show limits of statistical significance at the 95% confidence level; values outside bars are statistically significant. Root-mean-squared errors for the (c) 850- and (d) 700-hPa tropical winds at day 3 are shown.

a strong need to investigate the potential benefits of assimilating the lower-altitude RO observations for these purposes and, especially, to improve the characterization and understanding of the PBL structure. This is particularly important for more sensitive RO missions such as COSMIC-2, where the accuracy of the profiles in the low moist troposphere is expected to have improved from earlier RO missions. Since an accurate representation of the PBL is important to NWP, the goal of this study is to extract all possible information that these low-altitude observations can provide, rather than rejecting them outright.

We have implemented and tested a new forward operator to assimilate RO rays that penetrate layers of large vertical gradients of refractivity, including super-refractive layers. Compared to the previous NBAM forward operator, the new NABAM forward operator uses a different height coordinate system to estimate the bending angle. This reformulation results in a better forward simulation of the bending angle observations in the midlower troposphere. Furthermore, this new methodology enables the potential assimilation of lower-altitude RO observations to improve our understanding of the PBL region, especially the tropical maritime PBL. Prior to this new approach, the NCEP data assimilation system has not been able to assimilate rays at low tangent-point altitudes that have larger vertical gradients of atmospheric refractivity nor any rays below such larger vertical gradients of atmospheric refractivity. These cases include, but are not limited, to super-refraction. The new methodology described here offers the possibility to assimilate RO data to much lower altitudes in the atmosphere, excluding information at the

super-refracting levels themselves, though. A conservative implementation of NABAM in the NCEP global NWP system shows encouraging results in the lower tropical troposphere. Because of the use of the new formulation, temperature and wind forecast errors are reduced and the number of assimilated observations is increased.

With the new methodology, while it is possible to assimilate a larger number of low-altitude RO observations in the lower troposphere, the characterization of the errors of these deeper-penetrating rays is not well known. Here, we have adopted a conservative approach by slightly modifying the observation errors and quality controls applied to the observations. Future investigations will optimize the existing quality controls and tune the observation errors. This will include using an appropriately tuned adaptation of the nonlinear quality control technique (Purser 2018) that more optimally assigns a relative weighting on an observation-by-observation basis. Additionally, exploitation of the new methodology might also require implementation of the full tangent linear code, rather than the approximations adopted here. These research-to-operations activities will be coordinated with the Joint Effort for Data Assimilation Integration (JEDI; https://doi.org/10.25923/rb19-0q26).

In summary, this study has described the theoretical basis for the new methodology and presented a practical implementation for a numerical weather prediction data assimilation setting. Though using a conservative approach, benefits from this new methodology in the lower moist troposphere are already encouraging. This configuration sets up a baseline to build on by performing additional tuning and optimization of the quality control procedures. This is a necessary step for potential operational implementation of such enhanced assimilation algorithms so that higher performance in forecast skill over the current configuration can be demonstrated in a statistical sense, and we plan to do this in future studies.

Acknowledgments. The authors thank Dr. Ross Hoffman and two anonymous reviewers for their insightful comments and suggestions that helped improve the manuscript. We are also grateful to Drs. Sean Casey and Andy Tangborn for their valuable comments on the original version of this manuscript.

Data availability statement. Documentation and methodology used to support this study are available from Dr. Lidia Cucurull (Lidia.Cucurull@noaa.gov) at the National Oceanic and Atmospheric Administration.

REFERENCES

Abramowitz, M., and I. A. Stegun, 1970: *Handbook of Mathematical Functions with Formulas, Graphs, and Mathematical Tables.* National Bureau of Standards Applied Mathematics Series, Vol. 55, U.S. Government Printing Office, 1046 pp.

Anlauf, H., D. Pingel, and A. Rhodin, 2011: Assimilation of GPS radio occultation data at DWD. *Atmos. Meas. Tech.*, **4**, 1105–1113, https://doi.org/10.5194/amt-4-1105-2011.

Anthes, R. A., and Coauthors, 2008: The COSMIC/FORMOSAT-3 mission: Early results. *Bull. Amer. Meteor. Soc.*, **89**, 313–334, https://doi.org/10.1175/BAMS-89-3-313.

Ao, C. O., D. E. Waliser, S. K. Chan, J.-L. Li, B. Tian, F. Xie, and A. J. Mannucci, 2012: Planetary boundary layer heights from GPS radio occultation refractivity and humidity profiles. *J. Geophys. Res.*, **117**, D16117, https://doi.org/10.1029/2012JD017598.

Aparicio, J. M., and G. Deblonde, 2008: Impact of the assimilation of CHAMP refractivity profiles in environment Canada global forecasts. *Mon. Wea. Rev.*, **136**, 257–275, https://doi.org/10.1175/2007MWR1951.1.

Bauer, P., G. Radnóti, S. B. Healy, and C. Cardinali, 2014: GNSS radio occultation constellation observing system experiments. *Mon. Wea. Rev.*, **142**, 555–572, https://doi.org/10.1175/MWR-D-13-00130.1.

Bonavita, M., 2014: On some aspects of the impact of GPSRO observations in global numerical weather prediction. *Quart. J. Roy. Meteor. Soc.*, **140**, 2546–2562, https://doi.org/10.1002/qj.2320.

Born, M., and E. Wolf, 1964: *Principles of Optics: Electromagnetic Theory of Propagation, Interference and Diffraction of Light.* Pergamon Press, 856 pp.

Burrows, C. P., S. B. Healy, and I. D. Culverwell, 2014: Improving the bias characteristics of the ROPP refractivity and bending angle operators. *Atmos. Meas. Tech.*, **7**, 3445–3458, https://doi.org/10.5194/amt-7-3445-2014.

Cucurull, L., 2010: Improvement in the use of an operational constellation of GPS radio occultation receivers in weather forecasting. *Wea. Forecasting*, **25**, 749–767, https://doi.org/10.1175/2009WAF2222302.1.

——, 2011: Sensitivity of NWP model skill to the obliquity of the GPS radio occultation soundings. *Atmos. Sci. Lett.*, **13**, 55–60, https://doi.org/10.1002/asl.363.

——, 2015: Implementation of a quality control for radio occultation observations in the presence of large gradients of atmospheric refractivity. *Atmos. Meas. Tech.*, **8**, 1275–1285, https://doi.org/10.5194/amt-8-1275-2015.

——, and J. C. Derber, 2008: Operational implementation of COSMIC observations into the NCEP's global data assimilation system. *Wea. Forecasting*, **23**, 702–711, https://doi.org/10.1175/2008WAF2007070.1.

——, and R. A. Anthes, 2015: Impact of loss of microwave and radio occultation observations in operational numerical weather prediction in support of the U.S. data gap mitigation activities. *Wea. Forecasting*, **30**, 255–269, https://doi.org/10.1175/WAF-D-14-00077.1.

——, and M. J. Mueller, 2020: An analysis of alternatives for the COSMIC-2 constellation in the context of global observing system simulation experiments. *Wea. Forecasting*, **35**, 51–66, https://doi.org/10.1175/WAF-D-19-0185.1.

——, and S. P. F. Casey, 2021: Improved impacts in observing system simulation experiments by radio occultation observations as a result of data assimilation changes. *Mon. Wea. Rev.*, **149**, 207–220, https://doi.org/10.1175/MWR-D-20-0174.1.

——, J. C. Derber, and R. J. Purser, 2013: A bending angle forward operator for global positioning system radio occultation measurements. *J. Geophys. Res. Atmos.*, **118**, 14–28, https://doi.org/10.1029/2012JD017782.

——, R. A. Anthes, and L.-L. Tsao, 2014: Radio occultation observations as anchor observations in numerical weather prediction models and associated reduction of bias corrections in microwave and infrared satellite observations. *J. Atmos.*

Oceanic Technol., **31**, 20–32, https://doi.org/10.1175/JTECH-D-13-00059.1.

Culverwell, I. D., H. W. Lewis, D. Offiler, C. Marquardt, and C. P. Burrows, 2015: The radio occultation processing package, ROPP. *Atmos. Meas. Tech.*, **8**, 1887–1899, https://doi.org/10.5194/amt-8-1887-2015.

Duynkerke, P. G., and J. Teixeira, 2001: Comparison of the ECMWF reanalysis with FIRE I observations: Diurnal variation of marine stratocumulus. *J. Climate*, **14**, 1466–1478, https://doi.org/10.1175/1520-0442(2001)014<1466:COTERW>2.0.CO;2.

Feng, X., F. Xie, C. Ao, and R. A. Anthes, 2020: Ducting and biases of GPS radio occultation bending angle and refractivity in the moist lower troposphere. *J. Atmos. Oceanic Technol.*, **37**, 1013–1025, https://doi.org/10.1175/JTECH-D-19-0206.1.

Fjeldbo, G., A. J. Kliore, and V. R. Eshleman, 1971: The neutral atmosphere of Venus as studied with the mariner V radio occultation experiment. *Astron. J.*, **76**, 123–140, https://doi.org/10.1086/111096.

Garratt, J. R., 1994: *The Atmospheric Boundary Layer*. Cambridge University Press, 316 pp.

Hajj, G. A., E. R. Kursinski, W. L. Bertiger, L. J. Romans, and K. R. Hardy, 1994: Assessment of GPS occultations for atmospheric profiling. Preprints, *Seventh Conf. on Satellite Meteorology and Oceonography*, Monterey, CA, Amer. Meteor. Soc., J7–J10.

Healy, S. B., and J.-N. Thépaut, 2006: Assimilation experiments with CHAMP GPS radio occultation measurements. *Quart. J. Roy. Meteor. Soc.*, **132**, 605–623, https://doi.org/10.1256/qj.04.182.

——, J. R. Eyre, M. Hamrud, and J.-N. Thépaut, 2007: Assimilating GPS radio occultation measurements with two-dimensional bending angle observation operators. *Quart. J. Roy. Meteor. Soc.*, **133**, 1213–1227, https://doi.org/10.1002/qj.63.

Ho, S.-P., and Coauthors, 2020: Initial assessment of the COSMIC-2/FORMOSAT-7 neutral atmosphere data quality in NESDIS/STAR using in situ and satellite data. *Remote Sens.*, **12**, 4099, https://doi.org/10.3390/rs12244099.

Johnson, L. W., and R. D. Riess, 1982: *Numerical Analysis*. 2nd ed. Addison-Wesley, 663 pp.

Kursinski, E. R., G. A. Hajj, K. R. Hardy, J. T. Schofield, and R. Linfield, 1997: Observing Earth's atmosphere with radio occultation measurements using the global positioning system. *J. Geophys. Res.*, **102**, 23 429–23 465, https://doi.org/10.1029/97JD01569.

Lien, G.-Y., and Coauthors, 2021: Assimilation impact of early FORMOSAT-7/COSMIC-2 GNSS radio occultation data with Taiwan's CWB global forecast system. *Mon. Wea. Rev.*, **149**, 2171–2191, https://doi.org/10.1175/MWR-D-20-0267.1.

Lin, S.-J., 2004: A "vertically Lagrangian" finite-volume dynamical core for global models. *Mon. Wea. Rev.*, **132**, 2293–2307, https://doi.org/10.1175/1520-0493(2004)132<2293:AVLFDC>2.0.CO;2.

——, L. M. Harris, R. Benson, L. Zhou, J.-H. Chen, and X. Chen, 2017: Towards a unified prediction system from weather to climate scale. *Second Symp. on Multi-scale Atmospheric Predictability*, Seattle, WA, Amer. Meteor. Soc., 3.1, https://ams.confex.com/ams/97Annual/webprogram/Paper307703.html.

Poli, P., P. Moll, D. Puech, F. Rabier, and S. B. Healy, 2009: Quality control, error analysis, and impact assessment of FORMOSAT-3/COSMIC in numerical weather prediction. *Terr. Atmos. Oceanic Sci.*, **20**, 101–113, https://doi.org/10.3319/TAO.2008.01.21.02(F3C).

——, S. B. Healy, and D. P. Dee, 2010: Assimilation of global positioning system radio occultation data in the ECMWF ERA-Interim reanalysis. *Quart. J. Roy. Meteor. Soc.*, **136**, 1972–1990, https://doi.org/10.1002/qj.722.

Purser, R. J., 2018: Convenient parameterization of super-logistic probability models of effective observation error. NOAA/NCEP Office Note 495, 8 pp., https://doi.org/10.25923/kvmz-vf34.

Rennie, M. P., 2010: The impact of GPS radio occultation assimilation at the Met Office. *Quart. J. Roy. Meteor. Soc.*, **136**, 116–131, https://doi.org/10.1002/qj.521.

Rocken, C., and Coauthors, 1997: Analysis and validation of GPS/MET data in the neutral atmosphere. *J. Geophys. Res.*, **102**, 29 849–29 866, https://doi.org/10.1029/97JD02400.

Ruston, B., and S. B. Healy, 2021: Forecast impact of FORMOSAT-7/COSMIC-2 GNSS radio occultation measurements. *Atmos. Sci. Lett.*, **22**, e1019, https://doi.org/10.1002/asl.1019.

Schreiner, W. S., and Coauthors, 2020: COSMIC-2 radio occultation constellation: First results. *Geophys. Res. Lett.*, **47**, e2019GL086841, https://doi.org/10.1029/2019GL086841.

Soden, B. J., and I. M. Held, 2006: An assessment of climate feedbacks in coupled ocean–atmosphere models. *J. Climate*, **19**, 3354–3360, https://doi.org/10.1175/JCLI3799.1.

Sokolovskiy, S., 2003: Effect of superrefraction on inversions of radio occultation signals in the lower troposphere. *Radio Sci.*, **38**, 1058, https://doi.org/10.1029/2002RS002728.

Tatarskiy, V. I., 1968: Determining atmospheric density from satellite phase and refraction-angle measurements. *Izv. Atmos. Oceanic Phys.*, **4**, 401–406.

Von Engeln, A., and L. Teixeira, 2004: A ducting climatology derived from the European Centre for Medium-Range Weather Forecasts global analysis fields. *J. Geophys. Res.*, **109**, D18104, https://doi.org/10.1029/2003JD004380.

Wang, K.-N., M. de La Torre Juárez, C. O. Ao, and F. Xie, 2017: Correcting negatively biased refractivity below ducts in GNSS radio occultation: An optimal estimation approach toward improving planetary boundary layer (PBL) characterization. *Atmos. Meas. Tech.*, **10**, 4761–4776, https://doi.org/10.5194/amt-10-4761-2017.

Xie, F., S. Syndergaard, E. R. Kursinski, and B. M. Herman, 2006: An approach for retrieving marine boundary layer refractivity from GPS occultation data in the presence of superrefraction. *J. Atmos. Oceanic Technol.*, **23**, 1629–1644, https://doi.org/10.1175/JTECH1996.1.

——, D. L. Wu, C. O. Ao, E. R. Kursinski, A. J. Mannucci, and S. Syndergaard, 2010: Super-refraction effects on GPS radio occultation refractivity in marine boundary layers. *Geophys. Res. Lett.*, **37**, L11805, https://doi.org/10.1029/2010GL043299.